The influence of primary Cu_6Sn_5 size on the shear impact properties of Sn-Cu/Cu BGA joints

Z.Q. Li[1,*], S.A. Belyakov[1], J.W. Xian[1], C.M. Gourlay[1]

[1]Department of Materials, Imperial College London. SW7 2AZ. UK
* Corresponding author: zhenqi.li09@imperial.ac.uk

Abstract

A method is presented to control the size of primary Cu_6Sn_5 in ball grid array (BGA) joints while keeping all other microstructural features near-constant, enabling a direct study of the size of primary Cu_6Sn_5 on impact properties. For Sn-2Cu/Cu BGA joints, it is shown that larger primary Cu_6Sn_5 particles have a clear negative effect on the shear impact properties. Macroscopic fracture occurred by a combination of the brittle fracture of embedded primary Cu_6Sn_5 rods and ductile fracture of the matrix βSn. Cleavage of the Cu_6Sn_5 rods occurred mostly along (0001) or perpendicular to (0001) with some crack deflection between the two. The deterioration of shear impact properties with increasing Cu_6Sn_5 size is attributed to (i) the larger microcracks introduced by the brittle fracture of larger embedded Cu_6Sn_5 crystals; and (ii) the less numerous and more widely spaced rods when Cu_6Sn_5 are larger which makes them poor strengtheners.

Keywords: Reliability; Cu6Sn5; Pb-free solder; Electron backscatter diffraction

1. Introduction

Most Pb-free solder joints on Cu substrates solidify to contain up to 2 volume percent of primary Cu_6Sn_5 crystals in the bulk solder because of the combined influence of Cu substrate dissolution and the relatively large nucleation undercooling for βSn [1-5]. For typical peak reflow temperatures and cooling rates, the primary Cu_6Sn_5 grow into faceted hexagonal rods [1-3, 6-8], often with a hollow core [1, 2, 8-10], and can span almost the entire diameter of a ball grid array (BGA) solder joint [3, 8].

A large body of research has considered how the interfacial Cu_6Sn_5 reaction layer [11-14] affects the performance of solder joints where it has been found that, if fracture occurs through the Cu_6Sn_5 layer, the thickness influences the fracture toughness and generally the thicker the interfacial layer, the lower the fracture toughness [15-23]. However, much less research has explored the role of primary Cu_6Sn_5 crystals on solder joint performance and has generally focused on the role of primary Cu_6Sn_5 in tensile fracture. Tian et al. [24] showed that, during tensile loading, primary Cu_6Sn_5 undergo brittle fracture and these internal cracks act as sources of macro-cracks in the solder joint. Kim et al. found that long Cu_6Sn_5 rods have no apparent influence on the mechanical properties [25]. Quan et al. came to a similar conclusion for tensile behavior, however, they measured the highest strength from the joints containing these Cu_6Sn_5 rods [18]. Frear et al. showed that the role of primary Cu_6Sn_5 on the tensile properties depended on the temperature: at -196°C decohesion

2

occurred between Cu_6Sn_5 and the Sn matrix during deformation; At room temperature, fracture initiated at cleaved Cu_6Sn_5 rods, while at 125°C, primary Cu_6Sn_5 had little effect on tensile fracture [1].

Fundamental studies on the fracture of Cu_6Sn_5 have found that cleavage occurs on several planes and strain bursts were reported in the stress-strain curve [26-28]. Yu et al. showed that the fracture strength of Cu_6Sn_5 is higher along the c-axis than perpendicular to the c-axis [28]. This is in agreement with micrographs from crack patterns resulting from nanoindentation experiments. Nogita et al. showed that with increased indentation load, primary cracks formed perpendicular to the c-axis first and then secondary cracks were observed parallel to the c-axis of Cu_6Sn_5 rods [29-31].

Despite these past studies, the role of Cu_6Sn_5 in the bulk solder on the reliability of solder joints is much less clear than in the case of Ag_3Sn. For example, it has been shown that while small (<1 μm) eutectic Ag_3Sn particles improve crack resistance, hinder dislocation slip and reduce βSn grain boundary sliding [32-34], in contrast, primary Ag_3Sn usually form as large (100s of μm) plates (blades) in the bulk solder [35-38] and have been shown to negatively influence reliability. As large Ag_3Sn IMCs are brittle, they often fracture within the soft βSn matrix [25, 32, 33], providing an interfacial sliding path or decohesion from the βSn [25, 32] and act as secondary crack initiation sites [25]. Additionally, it has been shown that crack propagation can occur along the interface between βSn and an Ag_3Sn plate during thermal cycling [35].

While primary Ag_3Sn blades can be avoided in Sn-Ag-Cu/Cu solder joints by reducing the Ag content or suppressing the nucleation undercooling for βSn [35, 39], primary Cu_6Sn_5 generally cannot be avoided and will form for most solders on Cu substrates. This is because Cu substrate dissolution will bring the liquid to a hypereutectic composition (in the Cu_6Sn_5 primary phase field) where primary Cu_6Sn_5 forms irrespective of the initial composition or the nucleation undercooling for cooling rates typical of soldering [40].

It has been shown that the primary Cu_6Sn_5 size can be reduced either by controlling the heterogeneous nucleation of Cu_6Sn_5 (for example, by adding Al to introduce Cu_9Al_4 or $Cu_{33}Al_{17}$ which nucleates Cu_6Sn_5 [3, 41]) or by dilute Ni additions which strongly reduce the size of primary $(Cu,Ni)_6Sn_5$ particles[6]. However, it is unclear whether the size of primary Cu_6Sn_5 plays a role in shear impact reliability and whether it is worth controlling their size.

A challenge in measuring the influence of primary Cu_6Sn_5 size on the properties of BGA solder joints is that most factors that affect the size of primary Cu_6Sn_5, such as cooling rate, undercooling and microalloying, will also affect the lengthscale of the βSn dendrites and the eutectic IMCs which, themselves, have a large effect on properties. In this paper, we develop an experimental method to control the size of primary Cu_6Sn_5 while keeping the remaining microstructure near-constant. We then measure the influence of primary Cu_6Sn_5 size on the shear impact properties (at

constant volume fraction of Cu_6Sn_5) and explore their influence on the failure

mechanisms during shear impact loading.

2. Experimental Methods

Sn-2wt%Cu alloy was prepared by mixing 99.9wt%Sn and Sn-10wt%Cu ingots in a graphite crucible, heating and holding at 450℃ for 4 h, and then pouring into a steel mould. The composition of the alloy was analyzed by X-ray fluorescence (XRF) spectroscopy to be 2.1wt% Cu with impurities of Pb, Ag, Sb less than 0.02wt%, and Zn, Fe, Al, As, Cd less than 0.001wt%. The as-cast alloy was then rolled to foil with thickness ~0.03mm, punched into circular discs with diameter ~1.6mm and melted with a ROL1 tacky flux (IPC J-STD- 004) at ~350℃ on a hot plate to form solder balls with diameter 500±25 μm due to surface tension.

A method was developed to manipulate the primary Cu_6Sn_5 size in the initial freestanding solder balls and then largely maintain this primary Cu_6Sn_5 size in solder joints. To obtain the 'smallest' primary Cu_6Sn_5 size, liquid Sn-2Cu solder balls were quenched in ethanol from 350°C. To obtain a 'small' primary Cu_6Sn_5 size, liquid solder balls were solidified from 350°C under an air extractor. To obtain a 'medium' primary Cu_6Sn_5 size, balls cooled with an air extractor were aged at 150℃ for 2 weeks. To obtain the 'largest' primary Cu_6Sn_5 size, balls cooled with an air extractor were aged at 210℃ for 2 weeks.

Solder balls produced by each of the four procedures were then reflowed on standard FR4 test boards with 500μm Cu-OSP pads in a LFR400HTX TORNARDO reflow oven (Surface Mount Technology, Isle of Wight, UK) with thermal profile

6

shown in Fig. 1(a).

From Fig. 1 (b), it can be seen that under this reflow profile, the peak temperature is lower than the Cu_6Sn_5 liquidus temperature of Sn-2wt%Cu [42]. Thus, the primary Cu_6Sn_5 only partially remelt during reflow and the primary Cu_6Sn_5 size in the final joint retain features from the initial primary Cu_6Sn_5 in the solder ball. It can be seen from Fig. 1 (c) that partial melting of primary Cu_6Sn_5 leaves ~2 mass% primary Cu_6Sn_5 remaining at the peak temperature, while cooling to the eutectic temperature increases the amount of primary Cu_6Sn_5 to 2.8%, so that most of the Cu_6Sn_5 from the freestanding solder ball is not remelted during reflow. With this approach using Sn-2Cu, the primary Cu_6Sn_5 microstructures in the initial freestanding balls were largely maintained after soldering.

After reflow, the as-soldered joints were washed in ethanol in an ultrosonic bath to remove residual flux. BGA impact shear testing was performed on a DAGE-4000 following standard procedures in JESD22-B117B [43]. In order to investigate only the influence of primary Cu_6Sn_5 on the shear impact properties of solder joints, it is necessary to have solder joints fracture through the bulk solder and not the interfacial Cu_6Sn_5. Therefore, a 10mm/s displacement rate was selected. The hammer height was set at 50μm and the layout of the impact shear tester is illustrated in Fig. 2. At least 14 joints were tested for each of the four microstructure conditions.

The microstructures of both as-soldered joints and impact shear tested joints were studied. Cross-sections were prepared by mounting joints in Struers VersoCit resin,

grinding with SiC papers and polishing with SiO_2 suspension. Some samples were

deep etched in 5% NaOH and 3.5% orthonitrophenol in distilled H_2O to reveal the 3D

morphology of the primary Cu_6Sn_5. Fracture surfaces were examined without sample

preparation. Analytical scanning electron microscopy (SEM) was conducted in a Zeiss

Auriga field emission gun (FEG) SEM equipped with a Bruker e-Flash electron

backscatter diffraction (EBSD) detector and EBSD analysis was performed in Bruker

Esprit 2.1. Cu_6Sn_5 was indexed and analysed as the high temperature hexagonal

Cu_6Sn_5 polymorph [44, 45] since this phase is stable at the temperatures shown in Fig.

1(b) and (c).

3. Results and Discussion

3.1 Undeformed microstructures

Fig. 3 shows typical micrographs of the primary Cu_6Sn_5 in Sn-2wt%Cu/Cu joints produced from the four batches of solder balls containing Cu_6Sn_5 of different sizes. The first column are EBSD IPF-y maps of the Cu_6Sn_5 phase from typical cross-sections. It can be seen that the primary Cu_6Sn_5 have a wide range of orientations in each batch. The second column are BSE SEM images from the same cross-sections where the primary Cu_6Sn_5 appear dark grey. The number of primary Cu_6Sn_5 particles per unit area of cross-section was measured from EBSD maps of 4 samples per microstructure condition and the results are plotted in Fig. 4 (a). It can be seen that the joints with smallest primary Cu_6Sn_5 contain more than 4 times more primary Cu_6Sn_5 per unit area than the joints with largest primary Cu_6Sn_5. The number of Cu_6Sn_5 crystals were measured in Image J from BSE SEM images with information of the different Cu_6Sn_5 orientations from the EBSD maps. The third and fourth columns in Fig. 3 are SE-SEM images after partial dissolution of the matrix βSn at two magnifications. It can be seen clearly that the mean size (e.g. width) of the faceted Cu_6Sn_5 rods increases from (a) to (d). Combining this with the decreasing number of Cu_6Sn_5 particles from (a) to (d) in Fig. 3 and Fig. 4(a), it can be confirmed that the Cu_6Sn_5 rods are systematically larger and fewer (less numerous) from (a) to (d) in Fig. 3, and with a similar volume fraction since they have the same composition. Fig. 5 summarises the βSn microstructure and growth texture in un-deformed solder

9

joints from the four microstructure conditions, with increasing size of primary Cu_6Sn_5

from (a) to (d). The left column shows EBSD IPF-y maps of typical cross sections.

It can be seen that, in all cases, there are multiple orientations (colours) indicating

multiple βSn grains. The number of independent βSn grains was measured on

EBSD IPF maps from 4 joints for each condition, where grains were considered to be

independent if they were not related to other grains by twins, other special boundaries

or low angle boundaries [46]. The data are plotted in Fig. 4(b) where the error bars are

the standard deviations from the 4 samples for each condition. It can be seen that the

number of independent βSn grains was similar at 8.5 ± 0.2 for each microstructure

condition.

In Fig. 5, the middle column shows <001> pole figures for βSn grains in all joints

for each condition. These pole figures were made by combining all EBSD datasets

(at least 4) for each microstructure condition, ensuring that the y-direction was

perpendicular to the substrate in all cases. Note that, since βSn is tetragonal, it has

only one <001> direction in the northern hemisphere and, therefore, each βSn grain

contributes one point to the combined <001> pole figure. While the relatively small

number of grains from 4-7 samples with ~8 grains per sample precludes a meaningful

study of the statistics, it can be seen that in all microstructure conditions, the grains

have their c-axis oriented in a wide range directions and there is no clear texture.

The right column in Fig. 5 shows misorientation (MO) histograms which have

been compiled from all datasets for each microstructure condition. This was done

by summing the bins from each dataset so as to consider only misorientations within each joint and not consider misorientations between grains in different joints. Each plot also contains a Mackenzie curve which is the expected random misorientation distribution for tetragonal crystals. Each plot has the same following features: there is a peak at <10° corresponding to low angle boundaries, there are more misorientations with 10-50° than in a random distribution, and there are fewer misorientations with 50-100° than in a random distribution. It can be seen also that there are peaks in some of the MO plots, such as the 42-48° peak in Fig. 5(b); these occur because some joints had two large grains in a cross-section which gives a large MO peak in one sample. It is expected that these would not be present in the summed distributions if many more joints were added into these combined MO distributions.

By combining the number of independent grains in Fig. 4(b) with the textures and misorientation distributions in Fig. 5, it can be concluded that the number of βSn grains and the βSn growth texture is similar for all microstructure conditions. This confirms the success of the method developed to generate different primary Cu_6Sn_5 sizes while keeping the βSn microstructure near-constant. Additionally, the number of eutectic Cu_6Sn_5 particles per unit area was measured on BSE-SEM images for each condition and the results are plotted on Figure 4(b), where it can be seen that the number density of eutectic Cu_6Sn_5 particles is similar at each microstructure condition.

Note that the βSn texture in these Sn-2Cu/Cu joints (Fig. 5) is markedly different to

11

that in SnAg/Cu or SnAgCu/Cu BGA joints where there are usually only 1-3 βSn orientations that are all related by solidification twinning [4, 5, 47-49] (i.e. only one independent grain). It is also different to the texture of Sn-0.7Cu/Cu BGA joints which usually solidify with multiple columnar grains growing from the substrate[50] which leads to a strong <110> fibre texture in the y-direction [50, 51]. Examining the EBSD map in Fig. 5(d), it can be seen that there are some columnar βSn grains emanating from the substrate and that these have been blocked by near-equiaxed grains above. This suggests that βSn nucleation events have occurred ahead at the columnar front. This might indicate that the higher volume fraction of primary Cu_6Sn_5 has promoted βSn nucleation in the bulk solder in Sn-2Cu/Cu. Further work is required to prove the mechanism and explore whether this phenomenon can be used to usefully generate more βSn orientations in joints.

3.2 Impact shear properties

Typical examples of force-displacement curves from each microstructure condition are shown in Fig. 6. The examples shown are the median curve from at least 14 force-displacement curves obtained for each microstructure condition. It can be seen that the impact shear curves have two peaks. One initial small peak at a displacement of ~60μm, followed by a serrated increase in force up to the main peak. The shape of the curve is similar to past work at this displacement rate [52, 53].

Fig. 7 summarises the impact shear properties for joints with the four sizes of primary Cu_6Sn_5. It can be seen that both the maximum force and the energy absorbed decrease with increasing primary Cu_6Sn_5 size. The error bars represent the standard deviations from at least 14 samples for each condition. Note that the error bars for the smallest and small Cu_6Sn_5 joints do not overlap with the largest Cu_6Sn_5 joints, which highlights the significance of the result. From Fig. 3-7, it can be seen that, for equivalent βSn and eutectic microstructures and primary Cu_6Sn_5 volume fraction, increasing the size of primary Cu_6Sn_5 decreased the maximum force by 28% and decreased the energy absorbed by 39%. That is to say, when other microstructural variables are held near-constant, there is a clear negative effect of larger primary Cu_6Sn_5 particles on the shear impact properties of Sn-Cu/Cu BGA joints.

The width of primary Cu_6Sn_5 rods was measured on SE-SEM images of the fracture surfaces and a statistical overview of the measurements is given in Fig. 8 (a) and (b). In Fig. 8 (a), it can be seen that the standard deviation of the primary Cu_6Sn_5

13

width increased as the mean Cu_6Sn_5 width increased. This is thought to be because, during cooling at the end of reflow soldering, new primary Cu_6Sn_5 nucleate and grow in addition to the growth of incompletely melted primary Cu_6Sn_5, which gives a large range of primary Cu_6Sn_5 sizes in samples where the incompletely melted primary Cu_6Sn_5 are large.   Fig. 8 (b) presents box plots of the Cu_6Sn_5 width data; it can be seen that the lowest width, 25th percentile, 50th percentile, 75th percentile and highest width all increase as the mean Cu_6Sn_5 width increases.

Fig. 7 and Fig. 8 (a) have been combined into Fig. 8 (c) and (d) which shows the change in impact shear properties versus primary Cu_6Sn_5 width. There is a significant decrease in shear impact properties with increasing width of the primary Cu_6Sn_5. Fig. 8(e) and (f) show that the shear impact properties versus the number of primary IMCs within the joints (from Fig. 4(a)) for the four conditions. With increasing number of primary IMCs, both the maximum force and energy absorbed increase significantly.

Note that this result is specific to shear impact conditions where fracture is through the bulk solder and that different results might be expected at higher rate (e.g. 2000mm/s) where fracture typically involves the Cu_6Sn_5 layer.

3.3 Deformed microstructures

Typical cross sectioned micrographs of fractured solder joints are given in Fig. 9 . It can be seen that the fracture path for all joints was through the bulk solder, and that macroscopic fracture was by a combination of ductile fracture of the soft βSn matrix and brittle fracture of the hard embedded Cu_6Sn_5 rods. Thus, the Cu_6Sn_5 IMC layers did not strongly influence the fracture of the joints in this work.

To gain some insights into the initiation of fracture, interrupted impact tests were performed where the hammer was stopped at a certain displacement so that the microstructure could be studied and the events that occur early during impact testing could be deduced. Caution is required when interpreting interrupted tests as it was not possible to instantaneously halt the hammer motion and there may have been some βSn microstructure evolution between the time of impact and the time of EBSD measurements due to the high dislocation accumulation coupled with the high homologous temperature of $\sim 0.6 T_m$ at room temperature. Nevertheless, interrupted impact experiments provide useful information. Fig. 10 shows the typical results for an example where the hammer displacement was ~150 μm (~30% of the displacement of fully fractured joints) and where the impact direction was from left to right. Fig. 10(a) is a BSE-SEM image of a cross-section and Fig. 10(b) is an EBSD IPF-y map of βSn from the same area. In (b) it can be seen that βSn deformation is localized ahead of the hammer where the grains contain gradual changes in colour revealing a gradient of in-grain misorientation created by plasticity. Fig. 10(c)-(e) show typical regions where Cu_6Sn_5 particles have influenced the initiation and propagation of

15

microcracks. In Fig. 10(c), decohesion has occurred between a Cu_6Sn_5 rod and the

βSn matrix and propagated as a crack into the βSn matrix. In Fig. 10(d), brittle

fracture of a Cu_6Sn_5 rod followed by the opening displacement of this crack has

created a void in the ductile βSn matrix. In Fig. 10(e), a similar crack is beginning to

propagate from a cracked Cu_6Sn_5 rod into the βSn matrix. Thus, it can be seen that

brittle fracture of primary Cu_6Sn_5 crystals and decohesion between primary Cu_6Sn_5

and the βSn matrix both introduce internal microcracks early during shear impact.

Similar phenomena were observed after complete fracture. In Fig. 9 (e)-(h), it can

be deduced that brittle fracture of primary Cu_6Sn_5 crystals created microcracks which

opened (e.g. Fig. 9 (f)) and propagated in the βSn matrix. This is one factor behind the

deterioration of impact properties with increasing primary Cu_6Sn_5 size: The brittle

fracture of larger primary Cu_6Sn_5 rods creates a larger microcrack and, therefore, the

energy needed to open it and extend into the Sn matrix is smaller. Another factor is

that βSn plastic flow around larger Cu_6Sn_5 will open larger voids around the Cu_6Sn_5

which promotes βSn ductile tearing.

Fig. 11(a)-(d) presents typical fracture surfaces from the four microstructure

conditions. For all joints, the fracture surface is rough with the characteristics of

ductile tearing of βSn. Comparing Fig. 11 (a)-(d), it can be seen that the surfaces

have increasingly complex roughness from (a) to (d), corresponding to the larger and

fewer primary Cu_6Sn_5 from (a) to (d) as shown in the higher magnification images in

Fig. 11 (e)- (h). It was found that each fracture surface has two regions with

16

differently fractured primary Cu_6Sn_5. The region first touching the hammer is shown

in Fig. 11 (i). In this region, primary Cu_6Sn_5 are more vertical and brittle fracture

surfaces of numerous Cu_6Sn_5 grains can be seen, indicating that the embedded primary

Cu_6Sn_5 near the impact location underwent cleavage fracture.   There is also evidence

of decohesion between the Cu_6Sn_5 and βSn in some regions of Fig. 11 (i).   As the

hammer moves on, the fractured BGA surfaces become rougher and fragments of

fractured primary Cu_6Sn_5 rods are forced to be near parallel to the hammer direction

and plastically gouge trenches along the βSn fracture surface (Fig. 11 (j)). Therefore,

the plastic deformation of the βSn by gouging Cu_6Sn_5 fragments contributes to the

plastic work of ductile fracture in these joints.   Comparing rougher parts of solder

joints made with each microstructure condition, it was found that the fragments in the

smaller primary Cu_6Sn_5 microstructure conditions (e.g. smallest and small) tended to

align better with the hammer direction (Fig. 11 (k)) and appeared to gouge the βSn

fractured surface more.   This extra interaction between Cu_6Sn_5 fragments and the

βSn may be a further reason for the higher energy absorbed in samples with smaller

primary Cu_6Sn_5.

The fracture surfaces of individual primary Cu_6Sn_5 crystals were explored to gain

further insights in to the failure mechanisms. Primary Cu_6Sn_5 fracture surfaces which

were relatively parallel to the macroscopic fracture surface were chosen for EBSD

analysis.

Fig. 12(a)-(b) are SE-SEM images of typical fractured Cu_6Sn_5 rods from joints

containing 'medium' size primary Cu_6Sn_5 and Fig. 12(c) is a combined EBSD IPF-z

map of 11 fractured Cu_6Sn_5 where the fracture surface is near-perpendicular with the

z-direction in all cases (i.e. the normal to the fracture surfaces is approximately in the

z-direction). Note that the 11 fractured Cu_6Sn_5 come from different samples and

have been compiled into a single IPF-z map. The colours correspond to the

hexagonal colour legend in Fig. 12(d). It can be seen that 10 out of 11 fracture

surfaces have a green/blue colour and one has a red colour which corresponds to

cleavage approximately along prism planes and the basal plane respectively. This

result is plotted as an inverse pole figure with respect to the z-direction in Fig. 12(e).

The scatter in the data is largely because the Cu_6Sn_5 fracture surfaces are not

co-planar with the macroscopic fracture surface. Although only one basal fracture is

shown in Fig. 12 (c) (the red grain), this cleavage plane was widespread in the

samples. For example, inspection of the Cu_6Sn_5 rod fragments in Fig. 11(e)-(h) and

(j)-(k) shows that most fragments in these images fractured along their basal plane

(noting that Cu_6Sn_5 hexagonal rods are bounded by {10-10} facets with [0001] along

the rod [2, 40, 54]). Examples of prism fracture surfaces are shown in Fig. 12(a) and

(b).

As illustrated in reference [40], the {11-20} and {1-100} (the 2nd and 1st order

prism planes) are the closest-packed flat planes in hexagonal Cu_6Sn_5, and the basal

plane is the next closest packed, which agrees with the theory that the closest packed

planes are the preferred cleavage planes. The large number of basal fractures may

also be due to the shape of the long Cu_6Sn_5 rods (i.e. bending of a prismatic rod will favour basal fracture).

In some cases, it was found that the fracture path deflected as it propagated through a Cu_6Sn_5 crystal; either from a basal fracture to a prism fracture, from a prism fracture to a basal fracture or, sometimes, from one to the other and then back to the original fracture plane. For example, in Fig. 12(f) and (g), the crystal orientation can be determined from the {1-100} growth facets and [0001] growth direction of the Cu_6Sn_5 rods and deflection from basal to prism fracture can be inferred. This shows more than one cleavage plane is active in Cu_6Sn_5 fracture, which agrees with [30, 55]. Crack deflections are likely to be due to the combined effects of the crystallography of Cu_6Sn_5 (e.g. close-packedness of planes) and the orientation of the crystal relative to the hammer impact direction.

4. Conclusions

The influence of primary Cu_6Sn_5 size on shear impact properties has been investigated in 500μm BGA-type Sn-Cu/Cu joints. An effective method for manipulating the primary Cu_6Sn_5 size while keeping the remaining microstructure near-constant has been developed in which a high Cu content is used (2wt% Cu), the primary Cu_6Sn_5 size is manipulated in the initial freestanding solder balls (either by quenching during solder ball manufacture or by aging balls after manufacture), and this primary Cu_6Sn_5 size is largely maintained in solder joints because the peak reflow temperature (250 °C) is less than the Cu_6Sn_5 liquidus temperature so that the primary Cu_6Sn_5 only partially remelt.   This method was used to vary the Cu_6Sn_5 rod width from 3 - 12 μm and vary the number of primary Cu_6Sn_5 crystals per unit area of cross-section by a factor of 4.   BGA shear tests were performed on a DAGE-4000 bond-tester with 10mm/s hammer speed to ensure that fracture occurred through the bulk solder.

It has been found that the shear impact properties (maximum force and energy absorbed) decrease as the size of the primary Cu_6Sn_5 increases. That is to say, when other microstructural variables are held near-constant, there is a clear negative effect of larger primary Cu_6Sn_5 particles on the shear impact properties of Sn-Cu/Cu BGA joints.

Microstructure analysis revealed that brittle fracture of primary Cu_6Sn_5 and decohesion between primary Cu_6Sn_5 and the βSn matrix both introduce microcracks

early during shear impact. These microcracks then propagated into the soft βSn matrix by ductile tearing. The embedded primary Cu_6Sn_5 cleaved along (0001) and perpendicular to (0001), and Cu_6Sn_5 fragments then reoriented parallel with the hammer direction and continued to influence ductile fracture by gouging trenches into the βSn surface.

The deterioration of shear impact properties as the primary Cu_6Sn_5 rod size increases is attributed to (i) the larger microcracks introduced by cleavage of larger Cu_6Sn_5 rods and (ii) the smaller number and wider spaced Cu_6Sn_5 rods when the rods are larger.

Acknowledgements

References

1. D. Frear, D. Grivas, and J. Morris, J. Electron. Mater., 16: 181.(1987).
2. Y. Tian, R. Zhang, C. Hang, L. Niu, and C. Wang, Mater. Charact., 88: 58.(2014).
3. J.W. Xian, S.A. Belyakov, and C.M. Gourlay, J. Electron. Mater., 45: 69.(2016).
4. C.M. Gourlay, S.A. Belyakov, Z.L. Ma, and J.W. Xian, JOM, 67: 2383.(2015).
5. Z.L. Ma, S.A. Belyakov, and C.M. Gourlay, J. Alloy. Compd., 682: 326.(2016).
6. M.A.A. Mohd Salleh, S.D. McDonald, C.M. Gourlay, S.A. Belyakov, H. Yasuda, and K. Nogita, J. Electron. Mater., 45: 154.(2016).
7. M. Yang, Y. Cao, S. Joo, H. Chen, X. Ma, and M. Li, J. Alloy. Compd., 582: 688.(2014).
8. Z. Zhang, H. Cao, H. Yang, M. Li, and Y. Yu, J. Electron. Mater., 45: 5985.(2016).
9. M. Li, Z. Zhang, and J. Kim, Appl. Phys. Lett., 98: 201901.(2011).
10. R. Gagliano and M.E. Fine, JOM, 53: 33.(2001).
11. H.L.J. Pang, K.H. Tan, X.Q. Shi, and Z.P. Wang, Mater. Sci. Eng. A, 307: 42.(2001).
12. Q. Zhang, J. Tan, and Z. Zhang, J. Appl. Phys., 110: 014502.(2011).
13. J. Wang and H. Nishikawa, Microelectron. Reliab., 54: 1583.(2014).
14. L. Ching-Tsung, H. Chi-Shiung, C. Tao-Chih, and L. Ming-Kann. in *proccedings of 2007 International Microsystems, Packaging, Assembly and Circuits Technology*. (2007). pp. 58-61.
15. S.M. Hayes, N. Chawla, and D.R. Frear, Microelectron. Reliab., 49: 269.(2009).
16. H.-T. Lee, M.-H. Chen, H.-M. Jao, and T.-L. Liao, Mater. Sci. Eng. A, 358: 134.(2003).
17. Y.C. Chan, A.C.K. So, and J.K.L. Lai, Mater. Sci. Eng. B, 55: 5.(1998).
18. L. Quan, D. Frear, D. Grivas, and J.W. Morris, J. Electron. Mater., 16: 203.(1987).
19. Y.-H. Lee and H.-T. Lee, Mater. Sci. Eng. A, 444: 75.(2007).
20. A. Hirose, H. Yanagawa, E. Ide, and K.F. Kobayashi, Sci. Technol. Adv. Mat., 5: 267.(2004).
21. S. Ahat, M. Sheng, and L. Luo, J. Electron. Mater., 30: 1317.(2001).
22. X. Li, F. Li, F. Guo, and Y. Shi, J. Electron. Mater., 40: 51.(2011).
23. J.-W. Yoon, S.-W. Kim, and S.-B. Jung, J. Alloy. Compd., 391: 82.(2005).
24. Y. Tian, W. Liu, R. An, W. Zhang, L. Niu, and C. Wang, J. Mater. Sci. Mater. Electron., 23: 136.(2012).
25. K. Kim, S. Huh, and K. Suganuma, J. Alloy. Compd., 352: 226.(2003).

26.   L. Jiang and N. Chawla, Scr. Mater.,   63: 480.(2010).

27.   J. Yu, J. Wu, L. Yu, and C. Kao. in *proceedings of the 66th Electronic Components and Technology Conference (ECTC), 2016 IEEE*. (2016). pp. 1135-1140

28.   J. Yu, J. Wu, L. Yu, and C. Kao. in *proceedings of the Electronic Packaging and iMAPS All Asia Conference*. (2015). pp. 838-841.

29.   D. Mu, H. Huang, S. McDonald, J. Read, and K. Nogita, Mater. Sci. Eng., 566: 126.(2013).

30.   D. Mu, S. McDonald, J. Read, H. Huang, and K. Nogita, Current Opinion in Solid State and Materials Science,   20: 55.(2016).

31.   B. Philippi, K. Matoy, J. Zechner, C. Kirchlechner, and G. Dehm, Scr. Mater., 123: 38.(2016).

32.   M. Wang, J. Wang, H. Feng, and W. Ke, Mater. Sci. Eng. A,   558: 649.(2012).

33.   K. Kim, S. Huh, and K. Suganuma, Mater. Sci. Eng. A,   333: 106.(2002).

34.   F. Ochoa, J. Williams, and N. Chawla, JOM,   55: 56.(2003).

35.   D.W. Henderson, T. Gosselin, A. Sarkhel, S.K. Kang, W.-K. Choi, D.-Y. Shih, C. Goldsmith, and K.J. Puttlitz, J. Mater. Res.,   17: 2775.(2002).

36.   I.E. Anderson, J.W. Walleser, J.L. Harringa, F. Laabs, and A. Kracher, J. Electron. Mater.,   38: 2770.(2009).

37.   J. Gong, C. Liu, P.P. Conway, and V.V. Silberschmidt, Mater. Sci. Eng. A, 527: 2588.(2010).

38.   Z.L. Ma and C.M.Gourlay, J. Alloy. Compd.,   706: 596.(2017).

39.   S.K. Kang, D.-Y. Shih, N. Donald, W. Henderson, T. Gosselin, A. Sarkhel, N. Charles Goldsmith, K.J. Puttlitz, and W.K. Choi, JOM,   55: 61.(2003).

40.   J. Xian, S. Belyakov, M. Ollivier, K. Nogita, H. Yasuda, and C. Gourlay, Acta Mater., 126: 540.(2017).

41.   J. Xian, S. Belyakov, T. Britton, and C. Gourlay, J. Alloy. Compd.,   619: 345.(2015).

42.   Thermo-Calc, TCSLD Database version 3.0.(2015).

43.   JESD22-B117B 'Solder Ball Shear'

44.   B. Peplinski, G. Schulz, D. Schultze, and E. Schierhorn. in *Materials Science Forum*. 228: 577. (1996).

45.   K. Nogita, C. Gourlay, and T. Nishimura, JOM,   61: 45.(2009).

46.   A. Telang and T. Bieler, JOM,   57: 44.(2005).

47.   T.R. Bieler, *Lead free solder review*, in *Encyclopedia of Materials: Science and Technology*. 2010, Elsevier Ltd. pp. 1-12.

48.   L. Lehman, Y. Xing, T. Bieler, and E. Cotts, Acta Mater.,   58: 3546.(2010).

49.   B. Arfaei, N. Kim, and E. Cotts, J. Electron. Mater.,   41: 362.(2012).

50.   J. Xian, Z. Ma, S. Belyakov, M. Ollivier, and C. Gourlay, Acta Mater.,   123: 404.(2017).

51.   S. Belyakov, J. Xian, K. Sweatman, T. Nishimura, T. Akaiwa, and C. Gourlay,

J. Alloy. Compd., 701: 321.(2017).

52. H. Tsukamoto, T. Nishimura, S. Suenaga, and K. Nogita, Mater. Sci. Eng. B, 171: 162.(2010).

53. H. Tsukamoto, T. Nishimura, S. Suenaga, S.D. McDonald, K.W. Sweatman, and K. Nogita, Microelectron. Reliab., 51: 657.(2011).

54. Z.H. Zhang, M.Y. Li, Z.Q. Liu, and S.H. Yang, Acta Mater., 104: 1.(2016).

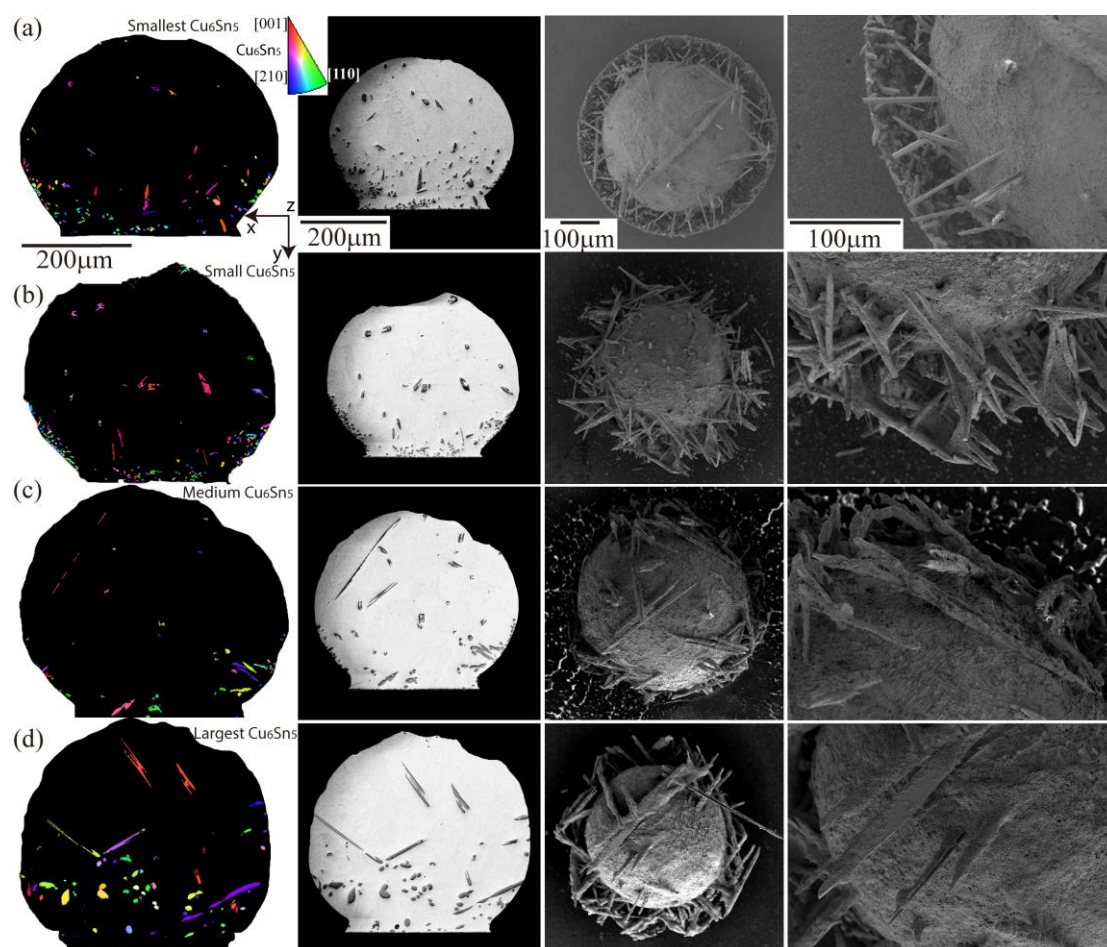55. D. Mu, H. Huang, S.D. McDonald, J. Read, and K. Nogita, Mater. Sci. Eng., 566: 126.(2013).

Figure captions
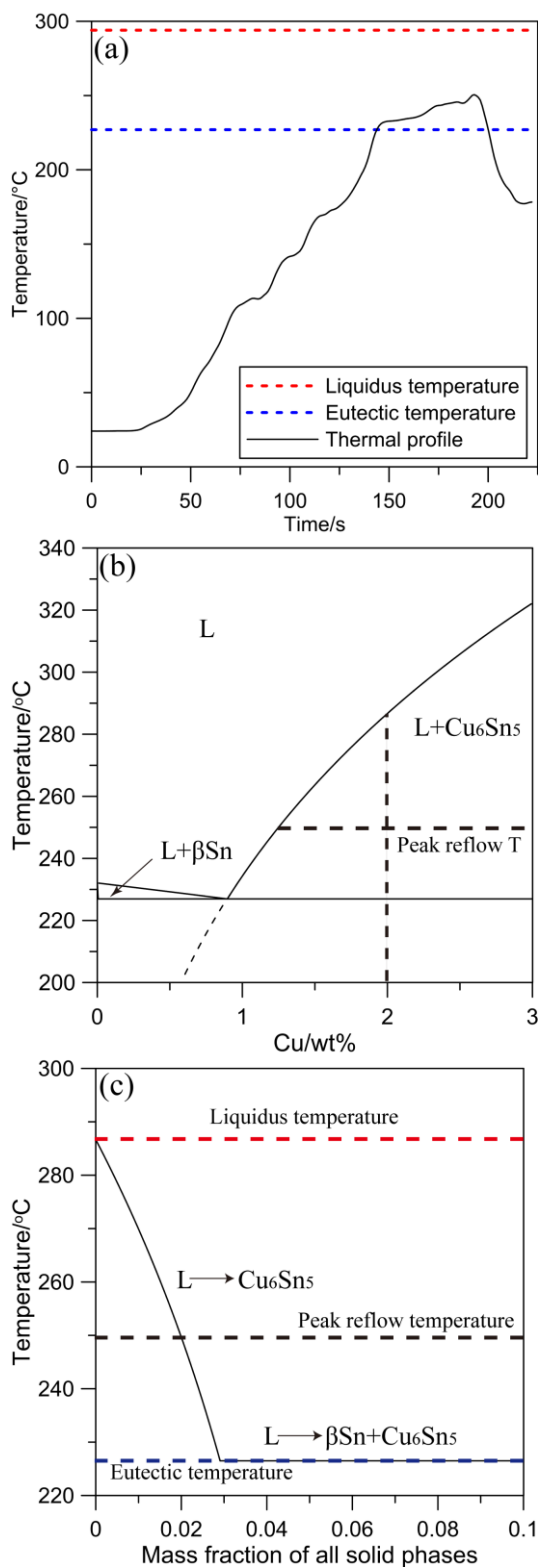
Fig. 1: (a) Thermal profile used for reflow soldering. (b) Sn-Cu phase diagram [42] highlighting the initial solder composition and the peak reflow temperature (c) Mass fraction of primary Cu_6Sn_5 as a function of temperature in Sn-2Cu [42].
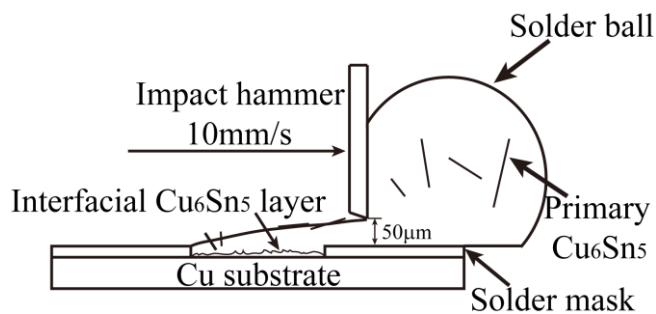
Fig. 2: Set up of shear impact testing on a DAGE4000.

Fig. 3: Overview of primary Cu_6Sn_5 in Sn-2Cu/Cu joints made with four sizes of primary Cu_6Sn_5, with increasing size of primary Cu6Sn5 from (a) to (d). The first and second columns are EBSD IPF-y maps and BSE-SEM images. The third and fourth columns are deep etched SE-SEM images of the primary Cu_6Sn_5 at two magnifications. Each column has a common scale bar.
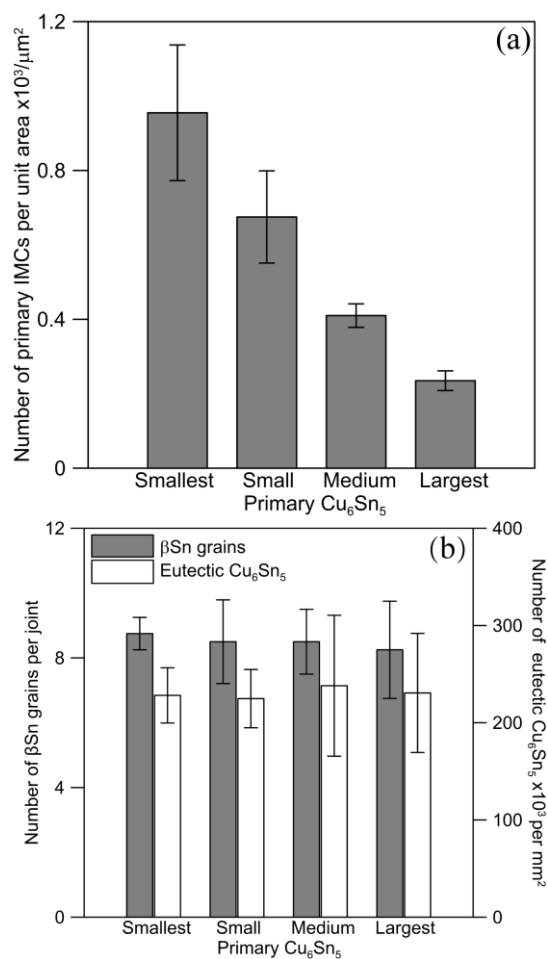
Fig. 4: Summary of microstructural measurements for each batch of Sn-2Cu/Cu joints. Bars are mean values, error bars are standard deviations. (a) Number of primary Cu6Sn5 per unit area. (b) Number of eutectic Cu6Sn5 particles per unit area, and number of βSn orientations per joint.
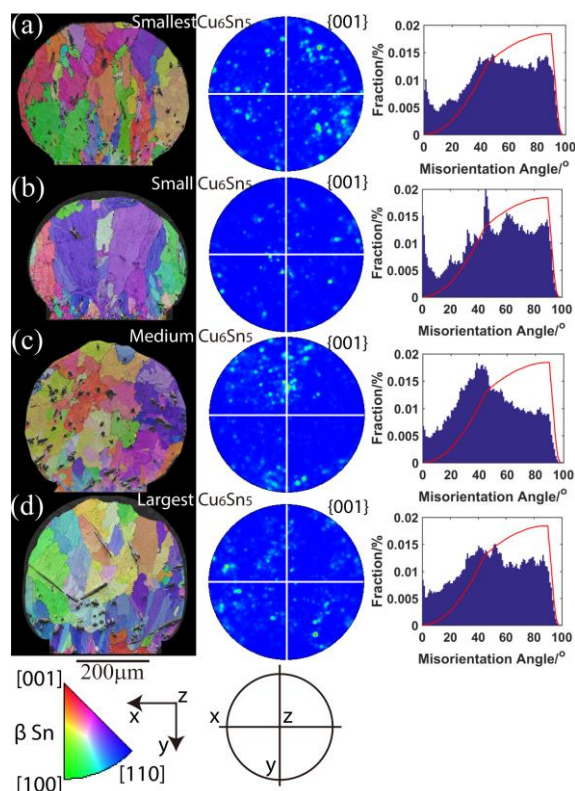
Fig. 5: Overview of βSn in Sn-2Cu/Cu joints, with increasing size of primary Cu6Sn5 from (a) to (d). The first column are EBSD IPF-y maps of typical joints. The middle column are {001} pole figures made by combining ≥4 EBSD maps for each microstructure condition. The third column are misorientation (MO) histograms, compiled from ≥4 joints for each microstructure condition. Mackenzie curves are superimposed on the MO distributions.
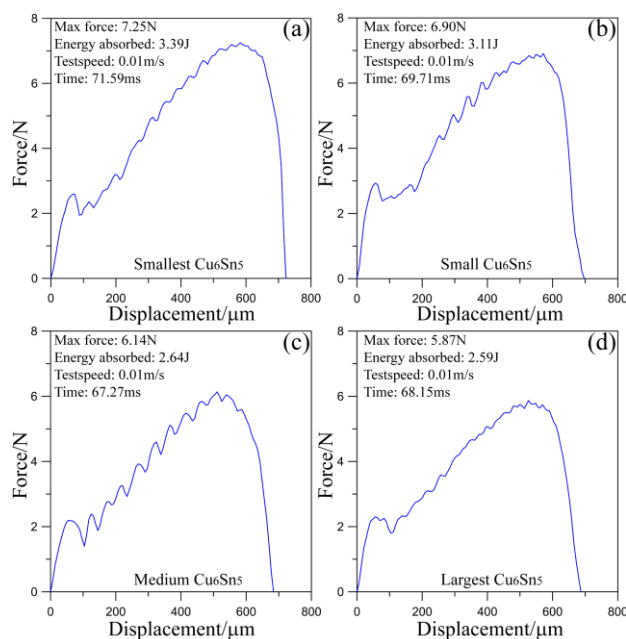
Fig. 6. Typical force-displacement curves from shear impact testing, with increasing

size of primary Cu6Sn5 from (a) to (d).
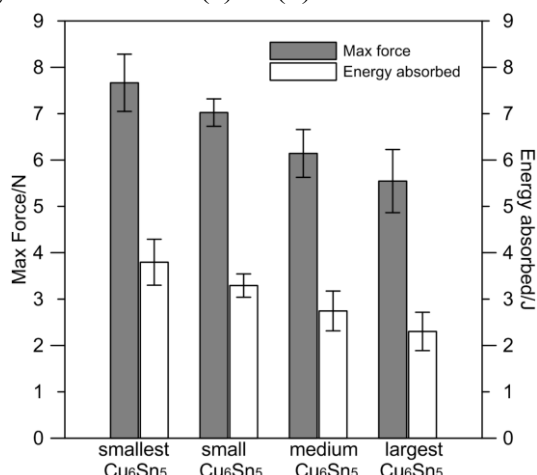
Fig. 7: Impact shear properties (maximum force and energy absorbed) of Sn-2wt%Cu/Cu with different size of primary Cu_6Sn_5.
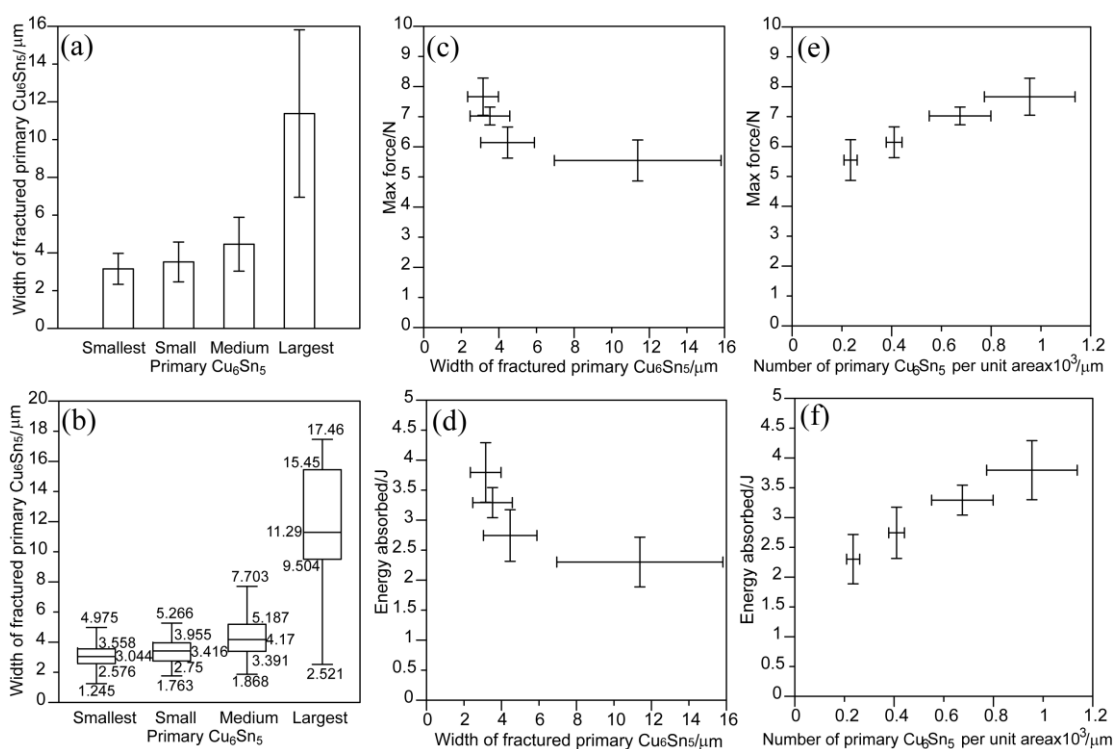

Fig. 8: (a) Width of fractured primary Cu_6Sn_5 on fracture surfaces for each microstructure condition. Bars are mean values, error bars are standard deviations. (b) The same data summarised in box plots. (c) Maximum force versus the width of fractured primary Cu_6Sn_5. (d) Energy absorbed versus the width of fractured primary Cu_6Sn_5. (e) Maximum force versus the number density of primary Cu_6Sn_5. (f) Energy absorbed versus the number density of primary Cu_6Sn_5.
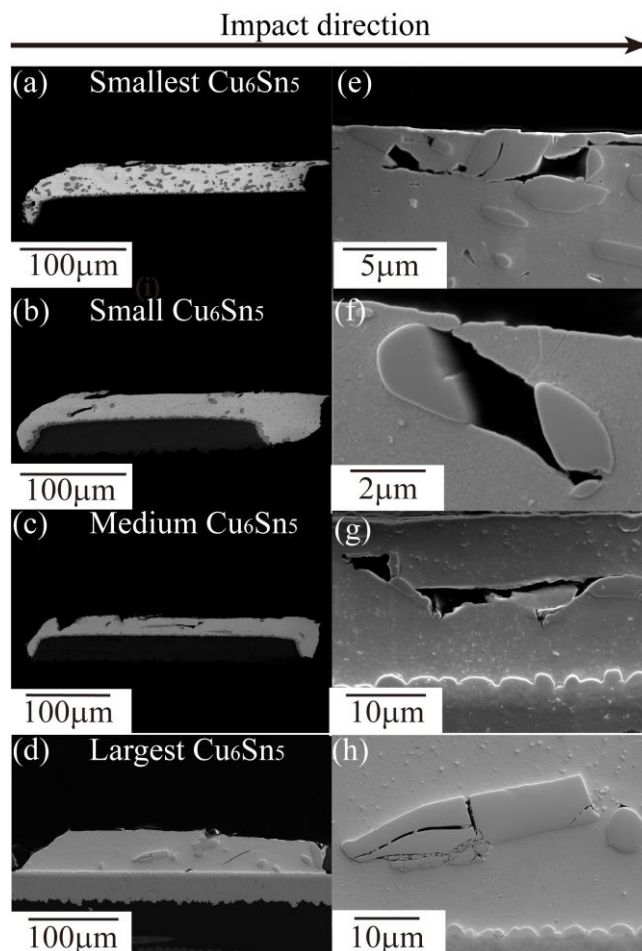
Fig. 9: Cross sections of fractured joints, with increasing size of primary Cu6Sn5 from top to bottom. (a)-(d) typical examples of the whole cross-section. (e)-(h): higher magnification images of primary Cu6Sn5 on and beneath the fracture surfaces.
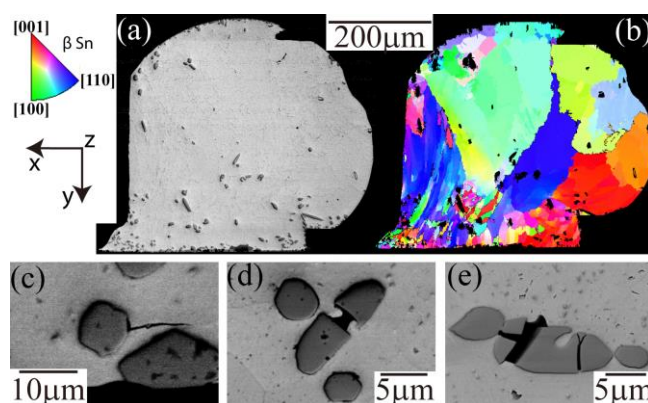
Fig. 10: Shear impact test interrupted at ~150μm. (a) BSE-SEM image of a cross-section. (b) EBSD IPF-y map of the same cross-section. (c)-(e) examples of decohesion between Cu_6Sn_5 and the βSn matrix, brittle fracture of primary Cu_6Sn_5, and the propagation of microcracks into the βSn.
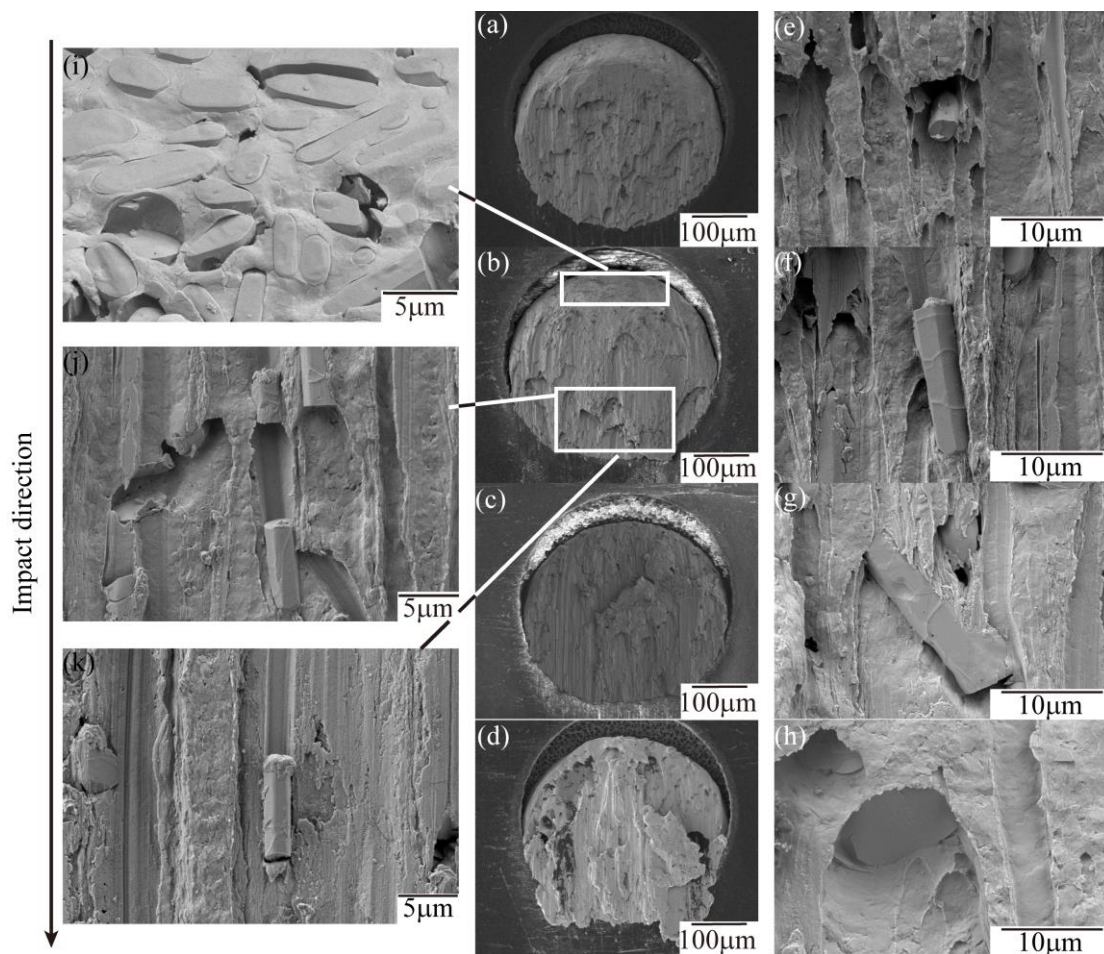
Fig. 11: Fracture surfaces of solder joints from batches with increasing size of primary Cu6Sn5 from (a) to (d). Typical examples of the varying Cu_6Sn_5 size are given in (e)-(h). (i)-(k) show typical features found at different locations of the fracture surfaces: (i) brittle fractured primary Cu_6Sn_5 at the 'front part' of the surface near to the initial hammer impact, (j)-(k) primary Cu_6Sn_5 fragments at the 'bottom part' of the surface.
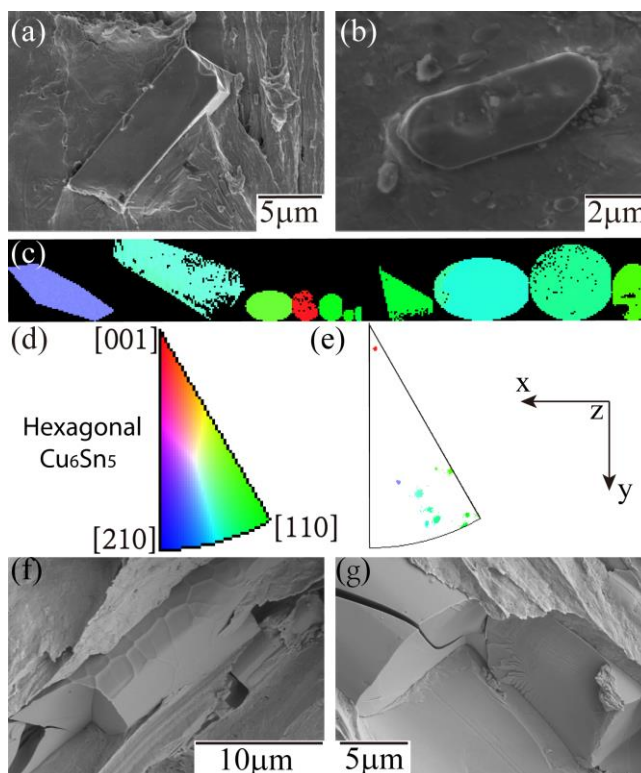
Fig. 12: (a)-(b) Typical Cu_6Sn_5 brittle fracture surfaces that are close to the plane of the macroscopic fracture surface.   (c) EBSD IPF-z map of 11 Cu_6Sn_5 fracture surfaces from different samples compiled into a single map.   (d) hexagonal IPF colour scale. (e) IPF-z for the 11 Cu_6Sn_5 crystals in (c). (f) and (g) examples of crack deflection from basal to prism fracture paths.